Journal of Materials Science: Materials in Electronics
https://doi.org/10.1007/s10854-020-04018-x

A comprehensive study on Cu_2SnS_3 prepared by sulfurization of Cu–Sn sputtered precursor for thin-film solar cell applications

Mohamed S. Abdel-Latif[1,2] · Wafaa Magdy[3,4] · Taichi Tosuke[5] · Ayaka Kanai[5] · Amr Hessein[1,6] · N. M. Shaalan[7,8] · Koichi Nakamura[9,10] · Mutsumi Sugiyama[5] · A. Abdel-Moniem[1,11]

Received: 19 March 2020 / Accepted: 14 July 2020

Abstract
In this work, a comprehensive study on the influences of the various synthesizing parameters of monoclinic Cu_2SnS_3 using the RF sputtering method, followed by the sulfurization process, is investigated. In particular, the impact of sputtering power and pressure on multi-material target Cu–Sn (compositional ratio Cu:Sn of 52:48%) was examined. All samples exhibited a monoclinic structure with similar split bandgaps around 0.9 eV. Increasing sputtering power showed direct effects on the sputtered Cu/Sn atoms ratio and the secondary phases obtained. The increase of sputtering pressure causes gas droplets and blistering on the film surfaces. The effects of changing the sulfurization temperature and the sulfur powder amount were also studied. The increase in the sulfurization temperature reduces the surface roughness, increases film crystallinity, and minimizes Cu-based secondary phases. The sulfur amount used during the sulfurization process showed a vital impact on film formation. Using a small amount of sulfur produced a partially sulfurized film that exhibited a poor performance solar cell. A power conversion efficiency of 1.94% is achieved with the optimized condition for the bare Cu_2SnS_3 without doping or heat treatment for the fabricated cell.

1 Introduction

As an alternative to waver-based silicon solar cells, thin-film solar cells (TFSC) have been subjected to extensive investigations to be cost-effective photovoltaic systems [1]. In particular, TFSC fabricated from chalcogenides semiconductors, such as Cu(In, Ga)Se_2 (CIGS) and cadmium telluride (CdTe), have significant market-share volumes [2]. The continuous increase in CIGS and CdTe TFSCs commercialization has led to significant advances in cell power conversion efficiencies (PCE). CIGS solar cell can be prepared with 23.4% PCE, while CdTe solar cell has reached

✉ Mohamed S. Abdel-Latif
mohamed.abdellatif@ejust.edu.eg;
mohamed.samir@f-eng.tanta.edu.eg

1 Department of Materials Science and Engineering, Egypt-Japan University of Science and Technology (E-JUST), New Borg El Arab City 21934, Alexandria, Egypt

2 Engineering Physics and Mathematics Department, Faculty of Engineering, Tanta University, 31511 Tanta, Egypt

3 Solid State Physics Department, National Research Center, Dokki, Giza 12311, Egypt

4 Solar Cell Lab, Center of Excellence for Advanced Sciences, National Research Centre, Dokki, Giza 12311, Egypt

5 Faculty of Science and Technology, Tokyo University of Science, 2641 Yamazaki, Noda 278-8510, Japan

6 Department of Mathematical and Physical Engineering, Faculty of Engineering (Shoubra), Benha University, 11614 Cairo, Egypt

7 Physics Department, Faculty of Science, Assiut University, 71516 Assiut, Egypt

8 Department of Physics, College of Science, King Faisal University, P.O. Box 400, Al-Ahsa 31982, Saudi Arabia

9 Department of Mechanical and Electrical System Engineering, Kyoto University of Advanced Science, 615-8577 Kyoto, Japan

10 Center for the Promotion of Interdisciplinary Education and Research, Kyoto University, 615-8540 Kyoto, Japan

11 Nanoscience Program, Institute of Basic and Applied Sciences, Egypt-Japan University of Science and Technology, New Borg El Arab City 21934, Alexandria, Egypt

Published online: 01 August 2020

22.1% PCE, overcoming that of polycrystalline Si solar cell [3]. However, Both CIGS and CdTe photovoltaics are prepared from rare-earth and high toxicity elements such as indium, cadmium, and tellurium, which would restrict their potential to fulfill the future photovoltaic market demands. As alternatives, earth-abundant, cheap, and non-toxic materials, such as Cu_2ZnSnS_4 (CZTS) and Cu_2SnS_3 (CTS), are emerging as good candidates for cost-effective and environment-friendly photovoltaics [4–7]. Although CZTS material possesses similar optical and electrical properties to CIGS, the best PCE achieved for the CZTS solar cell is only 12.6%, which is far below that of CIGS. This is mainly due to its structural complexity, as well as synthesizing pure phase kesterite CZTS compound is tricky due to the formation of secondary phases [8, 9].

CTS is a ternary semiconductor material with similar optoelectronic properties to CZTS and has a high potential for photovoltaic applications. CTS has p-type conductivity along with a high absorption coefficient ($> 10^4$ cm^{-1}) and excellent bandgap (0.9–1.4 eV) but has fewer elements than CZTS [10–12]. Thin films of CTS for solar cell application had been prepared by various physical and chemical deposition methods [13], Co-evaporation [14, 15], Pulsed laser deposition (PLD) [16], sputtering [17], chemical bath deposition (CBD) [18], chemical vapor deposition (CVD) [19]. The current highest PCE reported for CTS is 4.63%, which was achieved by Nakashima et al. using sequential evaporation to prepare the CTS film and by using Na doping [20]. In their study, the PCE of the CTS solar cell was increased from 1.1% for the undoped CTS to 4.63% when the alkali Na ions were incorporated into the CTS layer. Unfortunately, the highest PCE obtained for CTS is still very low when compared to the theoretical 30% PCE calculated for CTS-based solar cells [21]. The poor performance of the CTS solar cell is attributed to the lack of conventional deposition techniques that can accurately control the film's composition and homogeneity.

Advantageous from the other deposition techniques, RF sputtering technique can be used to deposit precisely controlled compositions, homogenous, uniform, and compact large-area films that are desired for industrial mass production. Despite the importance of the RF sputtering preparation method for the industrial field, there are several reports about sulfurization temperature optimization without a comprehensive study regarding the effects of the other sulfurization and sputtering parameters on the structural and optical properties of the CTS films prepared by RF sputtering [22–26]. Hence, mastering the RF sputtering parameter of the CTS film deposition before introducing dopant ions became a crucial factor in obtaining high-quality films and highly performance TFSC devices as well.

In this paper, a deep investigation of the impact of varying the sputtering parameters and sulfurization parameters on the physical properties, such as microstructure, morphology, and optical properties, of the CTS compound was introduced. We discuss important aspects related to the solar cell application when the CTS layer is prepared by the sputtering technique and the thin-film quality at various deposition conditions. The dependence of the CTS thin-film structural properties on the various synthesis parameters is well addressed. The optical absorption, bandgap energy, absorption coefficient, and the evolved absorption tails and Urbach energy with varying the deposition parameters are deeply studied. The photovoltaic performance of the TFSC device fabricated with an optimized CTS layer is demonstrated in the present study which is also correlated with previous CTS reports.

2 Experimental

2.1 Materials

The high-purity sputtering targets were purchased from Toshima Manufacturing, Japan. The molybdenum (Mo) target (3N, 99.9%) was used to sputter the back contact. The copper–tin (Cu–Sn) target (compositional ratio Cu:Sn 52%:48%) was 3N purity. Cadmium sulfate ($CdSO_4$, 99.0%) and thiourea ($SC(NH_2)_2$, 98%) were purchased from Kanto Chemical Co., INC. Japan. Ammonium hydroxide ($NH_4{\cdot}OH$, 25%) was obtained from Wako Pure Chemical Corporation, Japan. All other chemicals were from the reagent grade and used as received.

2.2 CTS film deposition

The fabricated CTS thin films were deposited on Mo-coated soda-lime glass (SLG/Mo) substrates by RF sputtering and sulfurization. Typically, the glass substrates were firstly cleaned for two rounds with deionized water and isopropanol for 40 min each with the aid of ultrasonication and dried under N_2 stream. Mo layer with a thickness of ~ 1 µm was then sputtered on the pre-cleaned substrates. The SLG/Mo substrates were then introduced into the RF sputtering chamber, and the Cu–Sn layer was sputtered from the Cu–Sn target and by using Ar gas. The sputtering power and chamber pressure were varied from 35 to 65 W and 1.4 to 2 Pa, respectively, listed in Table 1, without any intentional substrate heating. The deposition time was manipulated during the deposition process to obtain CTS layers with almost the same final thickness of ~ 1 µm. The thickness of the synthesized layers was measured through the cross section of the SEM image. The substrates with SLG/Mo/Cu–Sn stack were cut to 13×13 mm^2 pieces to fit the sulfurization tube.

The sulfurization process was performed in a tubular furnace. Four 13×13 mm^2 SLG/Mo/Cu–Sn samples were

Table 1 Sputtering and sulfurization parameters for CTS thin film deposited at a substrate temperature of RT

Process	Parameter effect	Sample name	RF sputtering parameters		Sulfurization parameters	
			RF power (W)	Pressure (Pa)	Temp. (°C)	Sulfur amount (mg)
Sputtering process	Power	*Po_35W*	35	1.8	580	100
		Po_50W	50			
		Po_65W	65			
	Pressure	*Pr_1.4Pa*	50	1.4	580	100
		Pr_1.8Pa		1.8		
		Pr_2.0Pa		2.0		
Sulfurization process	Temperature	*T_520°C*	50	1.4	520	10
		T_580°C			580	
		T_600°C			600	
	Sulfur amount	*S_10 mg*	50	1.4	580	10
		S_100 mg				100

put in a circular dish with sulfur powder centered between the substrates. The sulfurization tube was vacuumed at the beginning of the process and flushed with N_2 several times before starting the sulfurization process. The sulfurization process was performed at 10 °C/min heating rate under slow nitrogen flow and under a pressure of 10^5 Pa. The substrates were maintained at the desired sulfurization temperature for 2 h, and then cooled naturally. The sulfurization temperature and the sulfur amount were changed to study their effect on the CTS films, see Table 1.

2.3 Cell fabrication

The solar cells with configuration SLG/Mo/CTS/CdS/ZnO/ZnO:Al/Ni/Al were fabricated in this study. A CdS buffer layer of 60 nm thickness was deposited by chemical bath deposition (CBD) technique using a bath containing $CdSO_4$–thiourea–ammonium hydroxide aqueous solution; meanwhile, heating from room temperature to 66 °C. 30 min post-deposition annealing on a hot plate was done at 300 °C. The post-deposition annealing was beneficial for enhancing CdS optical properties by improving the contact between the p–n junction [27, 28]. The intrinsic ZnO layer of thickness 100 nm and Al-doped ZnO layer of thickness 300 nm were deposited by RF sputtering without intentional heating to complete the cell structure. Finally, a thick layer of the Al electrode is deposited on a thin layer of the Ni electrode layer by thermal evaporation technique. Each substrate was divided into 9 effective 3 mm^2 cells using mechanical scribing.

2.4 Characterization and measurements

Crystallographic structures and secondary phases generated during the samples manufacturing process were evaluated by X-ray diffraction (XRD) measurements (Rigaku, Ultima IV). Raman scattering measurements were performed on (JASCO, NRS-3200) Raman microscope with a 532 nm laser excitation source. Field emission scanning electron microscopy (FESEM, Hitachi S-4800) was used to investigate the samples' surface morphology and films' cross section. Transmission and reflectance spectra of the fabricated samples were recorded on (Hitachi, U-4100) UV–vis–NIR spectrophotometer. The photoluminescence spectra of fabricated cells (before electrode deposition) were detected using (Hamamatsu the compact NIR PL lifetime spectrometer C12132). Current density–voltage (*J–V*) characteristics of the fabricated solar cells were measured using a solar simulator (Bunkoukeiki Otento-SUN3) equipped with AM1.5 and under 100 mW/cm^2 illumination at 25 °C.

3 Results and discussion

3.1 Effect of RF sputtering power

The effect of changing sputtering power on the structural and optical properties of CTS thin films was studied. In single-element sputtering, the sputtering power has a direct impact on the deposition rate and film crystallinity [29]. Additionally, in the case of a multi-elements target, the sputtering power has the additional fact that it will control the film composition ratio. Thereby, for the sake of understanding of varying the sputtering power on the final film characteristics, RF powers of 35, 50, and 65 W were applied for depositing the CTS layer, while sputtering pressure was kept at 1.8 Pa. After deposition, all films were sulfurized at a temperature of 580 °C and a sulfur amount of 100 mg. The XRD patterns showed that all samples have a monoclinic CTS structure (PDF# 04-010-5719) with ($\bar{1}31/200$) preferential orientation at $2\theta = 28.44°$, as shown in Fig. 1a. The two low intensive peaks at 16.06° and 18.03° verified the attained monoclinic

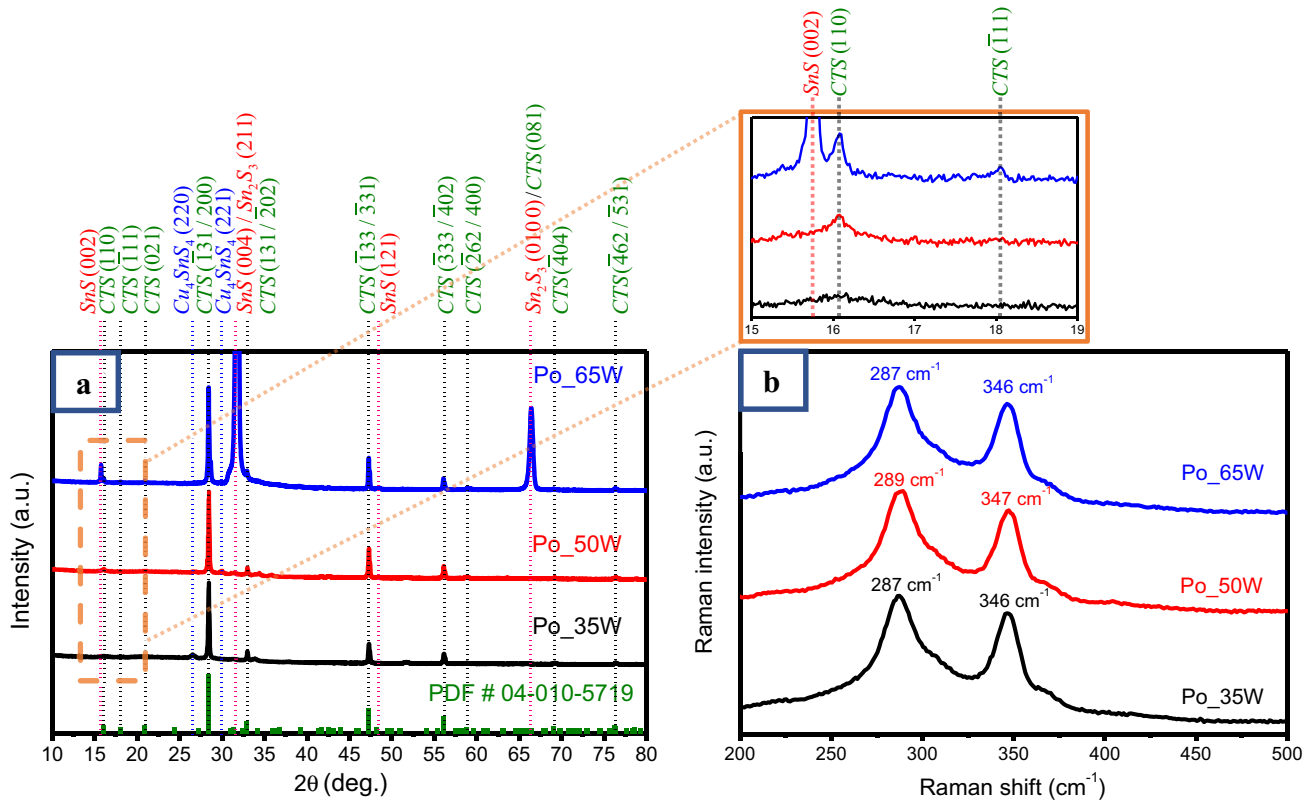

Fig. 1 **a** XRD and **b** Raman spectra of CTS thin films sputtered at different powers

crystal structure, which cannot be observed for the other CTS phases. Noticed, increasing sputtering power caused a change in the thin-film crystallinity as well as controlling Sn atoms released from Cu–Sn target to the substrate. Increasing the RF power is suggested to result in an increase in the Sn amount in the CTS layer. This suggestion was verified from the fact that the CTS sample prepared at low sputtering power *Po_35W* showed Cu-rich (Sn-poor) Cu_4SnS_4 (PDF# 27-0196) secondary phase. During the sulfurization process, the Cu–Sn layer surface is exposed to sulfur vapor that reacts with Cu–Sn precursor thin film to create intermediate phases SnS and CuS. They react together at sulfurization temperature larger at 580 °C to produce Cu–Sn–S compounds [30]. Hence, the initial Cu/Sn ratio in the deposited Cu–Sn layer has a crucial role in deciding which final primary and/or secondary phases shall be obtained. By increasing the sputtering power, Cu-poor (Sn-rich) secondary phases such as SnS (PDF# 53-0526) and Sn_2S_3 (PDF# 72-0031) became the prominent secondary phases as seen from the gradual increase of SnS peak located at 31.9°. The increase in the Sn amount with sputtering power was also additionally confirmed from the change in Cu/Sn ratio from 1.4 in the case of the *Po_35W* sample to 1.1 in the *Po_65W* sample as acquired from EDX measurements. Moreover, the Scherrer equation with $K = 0.9$ was employed to estimate the crystallite sizes for the three CTS prepared films [17]. The full width at half maximum (FWHM) of the preferential orientation peak was used in the calculation, and the crystallite sizes were estimated as 62, 60, and 53 nm for *Po_35W*, *Po_50W*, and *Po_65W*, respectively. This result implies that high RF power caused a formation of Sn-based secondary phases which affects CTS crystal growth. Additionally, due to the ambiguity associated with Cu–Sn–S compounds and the difficulty of phase identification [31], the Raman scattering technique was employed to identify the exact phase and structure of the prepared samples, and the obtained spectra are shown in Fig. 1b. The spectra of the three CTS thin films are characterized by the existence of two dominant Raman peaks at 290 cm^{-1} and 346 cm^{-1} assigned to the main A′ vibrational modes of monoclinic Cu_2SnS_3 phase. This result is in matching with the literature [30, 32, 33] and well matched with that obtained from the XRD results. It worth noting that, during Raman measurements of the *Po_65W* sample, the laser exposure spot was chosen as far as possible from the droplets and the SnS secondary phase region as indicated by yellow circles in Fig. 2d, to avoid the perturbation in CTS symmetry vibrational mode expected to occur due to the lattice-induced strain caused by the mismatch between CTS and SnS crystals.

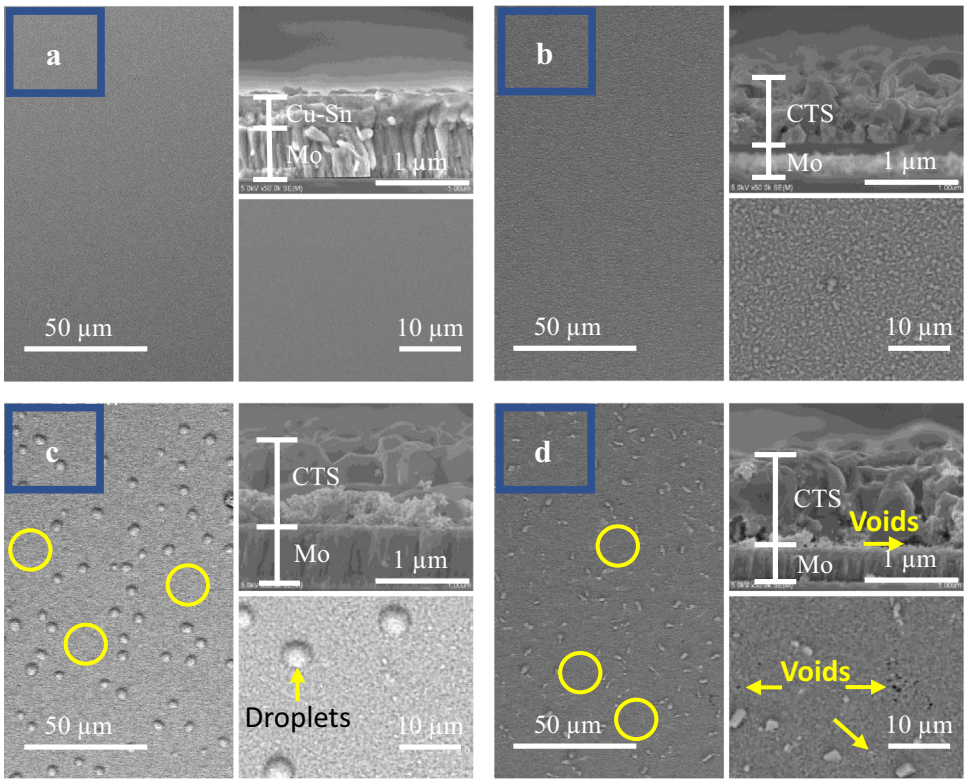

Fig. 2 Surface and cross-section morphology of **a** before sulfurization, **b** *Po_35W*, **c** *Po_50W*, and **d** *Po_65W* CTS thin films sputtered at different powers

The surface morphologies of the CTS thin-film samples before and after the sulfurization process were characterized employing SEM microscopy, and the obtained micrographs are presented in Fig. 2. It is seen from the micrograph of the as-prepared Cu–Sn layer in Fig. 2a that it has very smooth samples with uniform and compact cross section of ~ 0.5 µm in thickness. Also, good and void-free contact between the Cu–Sn layer and Mo back contact is noticed, which implies that 35 W sputtering power was adequate for the deposition of a high-quality Cu–Sn layer. Upon the sulfurization process, a noticeable volume expansion can be seen in Fig. 2b along with an increase in the surface roughness of the sulfurized film. The layer thickness was increased to ~ 1.2 µm due to introducing sulfur atoms and the formation of CTS compounds. The CTS sample prepared at higher sputtering power 50 W showed a larger thickness expansion of ~ 1.5 µm with lower surface roughness-associated blistering-like droplets. Because of increasing sputtering power from 35 to 50 W, the amount of sputtered Sn was increased. Consequently, the Sn-loss rate during the sulfurization process also increased, resulting in the attained blisters. However, it worthy of mentioning that both *Po_35W* and *Po_50W* samples maintained good and void-free contact with Mo back contact along with considerable grain sizes those preferred for solar cell applications. On the contrary, further power increasing to 65W caused almost no noticeable change in the CTS final thickness. However, the voids present on the *Po_65W* sample surface as well as at the CTS/Mo interface are seen as pointed out by the arrows in Fig. 2d. Additionally, Sn-based secondary phases (SnS and Sn_2S_3) can be seen as small white granules on the CTS film surface. Therefore, solar cell devices assembled with CTS deposited at high sputtering power are expected to show inferior performance due to high recombination rate and poor photoelectron collection efficiency at the back-contact electrode, besides plenty of secondary phase recombination centers are present as well.

Transmission and reflectance spectroscopy was utilized to evaluate the impact of RF sputtering power on the optical properties of CTS thin films, where the acquired spectra are displayed in Fig. 3a. Compared to the other two samples, the *Po_50W* sample showed the highest transmission and reflectance values, indicating its low light scattering because of the high phase purity and good crystallinity of the CTS layer. Moreover, the *Po_50W* sample has the most acute optical transition near the bandgap edge than the other two samples, which proves the low concentration of bulk defects within the CTS layer. Contrarily, the low crystallinity along with high surface roughness of *Po_35W* samples induce much light scattering, which resulted in the low attained transmission and reflectance spectra. As was expected from the XRD and SEM for the *Po_65W* sample, the existence of high-concentration Sn-based secondary phases at the sample surface, together with the evolved voids, are considered as the main reasons

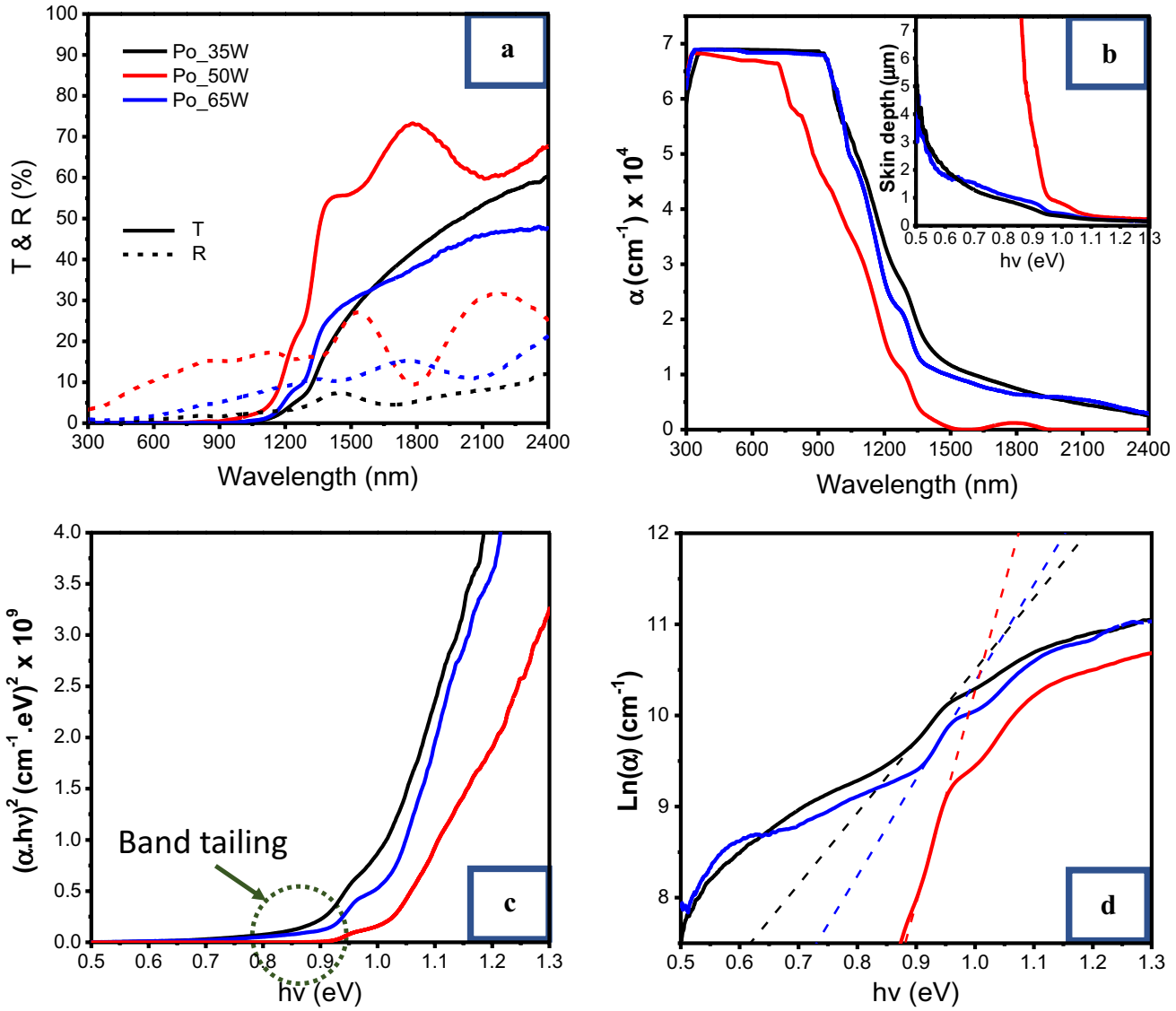

Fig. 3 Optical measurements: **a** transmission (continuous line) and reflectance (dashed line), **b** absorption coefficient intersected by Skin depth (small graph), **c** Tauc's plot (direct transition n = 1/2), and **d** Urbach energy of CTS thin films sputtered at different powers

behind the much lower transmission and reflectance spectra obtained for the *Po_65W* sample. Distinguishable between the three samples, the interference fringes are only seen in the transmission spectrum of the *Po_50W* sample reflecting its smooth surface [34], in correlation with the SEM and XRD measurements.

The absorption coefficient (α) of the CTS thin films was calculated according to the equation of the transmission (T) and reflectance (R) [35, 36]:

$$\alpha = \frac{1}{t}\ln\left[\frac{(1-R)^2}{2T} + \sqrt{\frac{(1-R)^4}{4T^2} + R^2}\right], \quad (1)$$

where t is the film thickness. The absorption coefficients as a function of wavelength $\alpha(\lambda)$ for the three samples are shown in Fig. 3b, whereas the values of α around the optical band edge are presented in Table 2. Although the three samples showed nearly the same values of $\alpha(\lambda)$ in the visible region, the *Po_50W* sample has the lowest value of α through the entire wavelength range. This result is well matched with the above discussion that *Po_50W* has fewer defects compared to other samples. The relatively higher values of α calculated for *Po_35W* and *Po_65W* samples, especially in the NIR region, are attributed to the abundance of secondary phases and also to the structural defects that exist in these samples [37]. Hence, it suggested that the fabrication of a thicker defect-free CTS layer would be beneficial for capturing as

Table 2 Sputtering power effect on CTS film parameters

Sample	Crystallite size (nm)	E_g (eV)	α at E_g ($\times 10^4$ cm^{-1})	δ at E_g (μm)	E_U (meV)
Po_35W	62.5	$E_{g1} = 0.88$ $E_{g2} = 0.97$	1.66 2.95	0.6 0.34	127.1
Po_50W	60	$E_{g1} = 0.92$ $E_{g2} = 1.01$	0.29 1.26	3.42 0.79	42.8
Po_65W	53	$E_{g1} = 0.9$ $E_{g2} = 1.0$	1.19 2.31	0.85 0.44	93.8

much as possible of the incident sunlight. However, too thick layer means a longer distance that photoelectrons should travel before extraction at the p–n junction interface, which increases the probability of photoelectron loss via recombination. In this regard, skin depth (sometimes called penetration depth δ) is another valuable optical factor that defines the deepness beneath the film surface at which the light intensity will fall to 1/e of its original incident value. Skin depth is governed by incident photons' frequency and semiconductor conductivity, which is dependent on bandgap energy [38, 39]. Skin depth was calculated from the reciprocal of the absorption coefficient as follows [38, 39]:

$$\delta = \frac{1}{\alpha}. \tag{2}$$

As a result, the skin depths of the three samples in the inset of Fig. 3b plotted against photon energy (eV) showed that the *Po_50W* sample has the highest δ thickness, especially around optical bandgap energy.

CTS is a direct bandgap semiconductor with p-type conductivity. The direct bandgap energies of the fabricated samples were calculated using Tauc's plot, as shown in Fig. 3c, by extrapolating the linear part of the relationship between $(\alpha h\nu)^2$ and the incident photons energy ($h\nu$) [37]. Nonetheless, due to the reduced symmetry of the CTS monoclinic phase, the splitting of the upper valence band (VB) states is likely occurring by approximately a hundred meV. According to Wild et al. study, valence band splitting (VBS) is expected to show double or triple absorption edges on the optical spectra of monoclinic CTS because transitions from all split VB states to the conduction band minimum (CBM) at the Brillouin zone center (Γ) are allowed [34]. In our case, two transitions were observed at ~ 0.9 eV and 1.0 eV in Tauc's plot in Fig. 3c, corresponding to two bandgaps for each CTS sample. The exact values of the bandgap energies were extracted and are listed in Table 2. The slight variation in the bandgap values for the three samples confirms our findings from the XRD measurements that changing RF sputtering power almost does not affect the CTS grain size.

Energy band tailing is another basic information that can be extracted from the optical spectra to investigate the optical quality of the prepared samples. Tails in the bandgap are induced from localized states in the forbidden gap above VBM and below CBM and usually observed in samples suffering from the structural disorder, defects, and impurities. These localized trap states absorb light energy in the low-energy region, i.e., below the bandgap absorption. Urbach rule is an empirical equation that relates to the absorption coefficient (α) and photon energy ($h\nu$) exponentially [40, 41]:

$$\alpha = \alpha_o \exp\left(\frac{h\nu}{E_U}\right), \tag{3}$$

where α_o is material dependent constant, and E_U is called Urbach energy denoting the tailing width into the bandgap. By rearranging Eq. (3):

$$\ln \alpha = \ln \alpha_o + \frac{h\nu}{E_U}. \tag{4}$$

Thus, Urbach tail energy can be calculated from the reciprocal of the slope of the straight-line fitting near the band edge when ln(α) is drawn on the vertical axis and $h\nu$ is drawn on the horizontal axis, as shown in Fig. 3d.

From the calculated Urbach energies in Table 2, the CTS sample *Po_50W* showed the lowest tailing energy among the three samples ~ 42.8 meV, which also implies the high optical quality of this sample and a high degree of crystalline ordering.

In brief, the 50 W RF sputtering deposition power has shown its capability for producing CTS thin films with acceptable quality in comparison with the low or even the high deposition power. The slight Cu-poor composition deposited at the 50 W from Cu–Sn target was proved to be a favorable composition due to the unwanted loss of Sn atoms during sulfurization. The careful structural and optical data analysis has led to monoclinic CTS thin film with the minimum content of secondary phases, and proper structural defects were successfully prepared at this sputtering power that is preferred for high-performance devices.

3.2 Effect of RF sputtering pressure

The influences of sputtering pressure variation on the structural and optical properties of the CTS films will be considered in this section. The values of the sputtering pressures were changed from 1.4 to 2 Pa, while the sputtering power was kept at 50 W. Afterward, the films were sulfurized at a temperature of 580 °C and with a sulfur amount of 100 mg. The analysis of the XRD measurements shown in Fig. 4a reveals that changing the pressure of the Cu–Sn sputtering process has no significant effect on the CTS phase as well as on the nature of the obtained secondary phases. Conversely, SEM micrographs presented

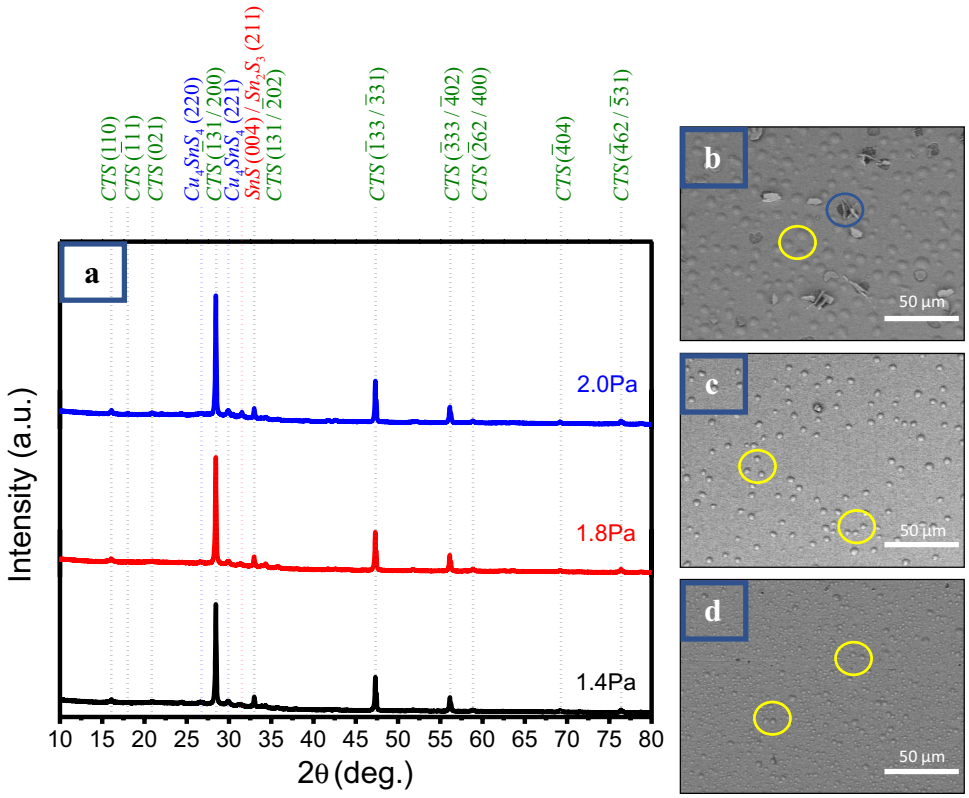

Fig. 4 **a** XRD pattern and surface SEM images of CTS thin films sputtered at different pressure conditions **b** 2.0 Pa, **c** 1.8 Pa, and **d** 1.4 Pa

in Fig. 4b–d declare a considerable change in the CTS surface morphology upon changing the sputtering pressure. Increasing sputtering pressure led to an increase in the attained blisters density observed on the CTS thin-film surfaces along with a significant increase in their size. Similar results were also reported for sputtered CdTe thin films by Kaminski et al., which were attributed to the argon gas trapped during the sputtering process because of the highly used argon pressure [42]. Furthermore, P. Björkman and his group stated that increasing the substrate temperature during the deposition process or changing the inert gas with bigger atom size gas such as Krypton will reduce the blister formation [43]. Herein, increasing the sputtering pressure does not only increase the amount of trapped argon gas but also causes an increase in the deposited Sn ratio. As a consequence, and due to the high sulfurization temperature of 580 °C, the trapped argon diffuses to the film surface, creating surface gas droplets, indicated by yellow circles in Fig. 4b–d. Also, by increasing the sputtering pressure, the rate of Sn atoms loss by evaporation during the sulfurization should increase. However, the formation of gas droplets may represent a barrier against Sn atoms loss, causing Sn atoms to accumulate, which resulted in the large voids, shown by blue circles in Fig. 4b and big blisters detected when reaching 2.0 Pa. As the surface blisters and voids increase, it will be a challenge to form a perfect and pinhole-free p–n junction at CTS/CdS interface which is essential to fabricate a high-performance CTS thin-film solar cells.

The optical measurements shown in Fig. 5 and summarized in Table 3 confirm the independence of CTS optical bandgap on the sputtering pressure, which is a subsequent result of the similar crystallinity of the three samples. Although the CTS thin film prepared at 1.4 Pa attained 68.8-meV Urbach energy, it exhibits the highest absorption coefficient and the appropriate skin depth at the fundamental optical bandgap among the three samples. Based on this above analysis, intermediate RF sputtering power of 50 W alongside with lower working pressure of 1.4 Pa is chosen as the preferred deposition pressure throughout the rest of this study.

3.3 Effect of sulfurization temperature

In this part of the study, the effect of changing sulfurization temperature on the structural and optical properties of CTS thin films will be discussed. Three CTS thin-film samples were prepared at three different sulfurization temperatures, namely, 520 °C, 580 °C, and 600 °C with a heating ramp of 10 °C/min. The substrates were maintained at the desired sulfurization temperature for 2 h, and then they were let to cool naturally. The other preparation conditions, such as the RF sputtering power, the sputtering pressure, and sulfur source amount, were kept fixed at 50 W, 1.4 Pa, and 10 mg,

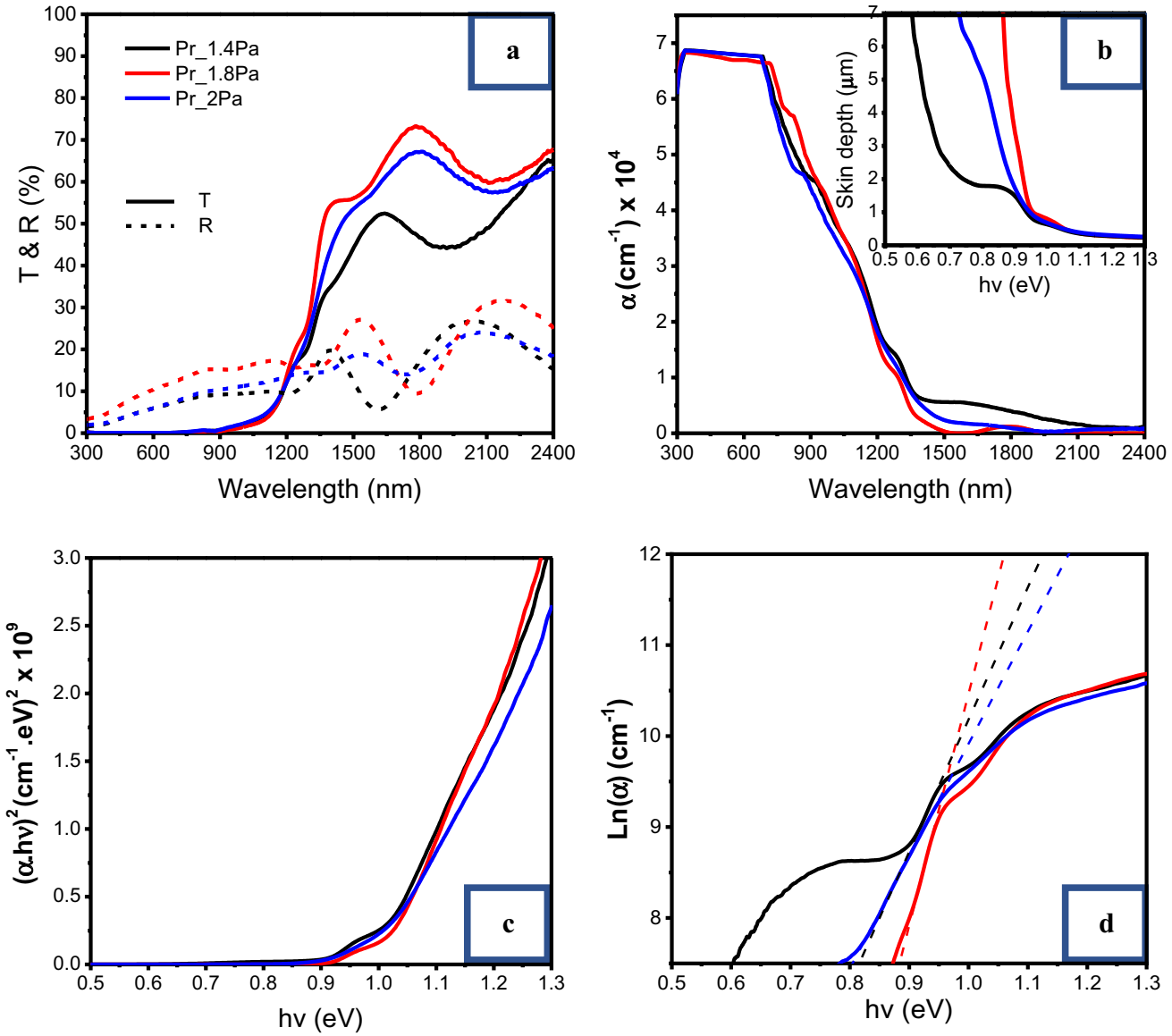

Fig. 5 Optical measurements: **a** transmission (continuous line) and reflectance (dashed line), **b** absorption coefficient intersected by Skin depth (small graph), **c** Tauc's plot (direct transition $n = 1/2$), and **d** Urbach energy of CTS thin films sputtered at different pressures

Table 3 Sputtering pressure effect on CTS film parameters

Sample	Crystallite size (nm)	E_g (eV)	α at E_g ($\times 10^4$ cm^{-1})	δ at E_g (μm)	E_U (meV)
Pr_1.4Pa	62.8	$E_{g1} = 0.90$ $E_{g2} = 0.99$	0.64 1.58	1.5 0.63	68.8
Pr_1.8Pa	60	$E_{g1} = 0.91$ $E_{g2} = 1.01$	0.29 1.26	3.42 0.79	39.2
Pr_2.0Pa	66	$E_{g1} = 0.90$ $E_{g2} = 0.99$	0.56 1.52	1.75 0.65	80.9

respectively. From the XRD patterns shown in Fig. 6a, all three samples showed a monoclinic CTS structure with an obvious increase in the CTS crystallinity with increasing in the sulfurization temperature. The enhancements in the crystallinity can be inferred from the increase in the intensity of CTS diffraction peak at 28.4° concerning the intensities of secondary phase diffraction peaks. This result was also accompanied by a significant increase in the CTS crystallite

size as can be seen from Table 4. Furthermore, monoclinic CTS is also identified from Raman measurements in Fig. 6b. The two characteristic Raman peaks of the CTS monoclinic phase at ~289 cm^{-1} and ~348 cm^{-1} were present in the spectra acquired from the three samples. However, the Raman peaks of the *T_520 °C* sample were much broader compared to those of the other two samples which implies the improvement in the structural ordering of the CTS with increasing the sulfurization temperature. Additionally, surface and cross-section SEM images in Fig. 7 showed that the higher the sulfurization temperature, the better the surface roughness.

Figure 8 shows the optical measurements of the three samples, and the estimated optical properties are summarized in Table 4. The transmission and absorption spectra in Fig. 8a and b, respectively, showed that the low-temperature

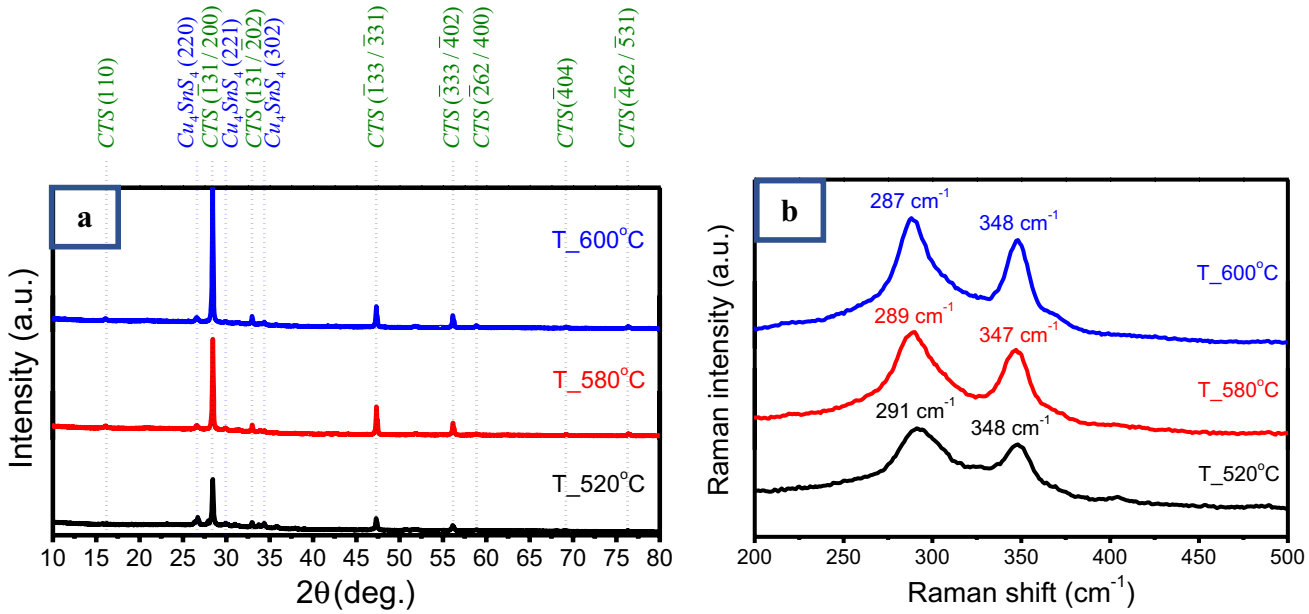

Fig. 6 **a** XRD and **b** Raman spectra of CTS thin films sulfurized at different temperatures

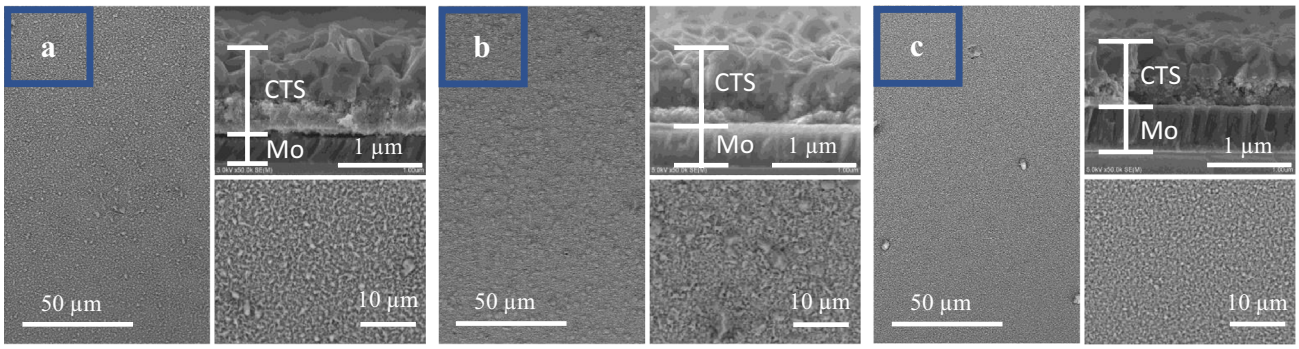

Fig. 7 Surface and cross-section morphology of CTS thin films sulfurized at different temperatures **a** 520 °C, **b** 580 °C, and **c** 600 °C

Table 4 Sulfurization temperature effect on CTS film parameters

Sample	Crystallite size (nm)	E_g (eV)	α at E_g (10^4 cm^{-1})	δ at E_g (µm)	E_U (meV)
T_520°C	48.6	$E_g = 0.97$	2.92	0.33	247.12
T_580°C	62.5	$E_{g1} = 0.90$ $E_{g2} = 1.00$	1.08 2.27	0.92 0.41	79.05
T_600°C	65.9	$E_{g1} = 0.91$ $E_{g2} = 1.01$	0.77 1.85	1.30 0.54	64.79

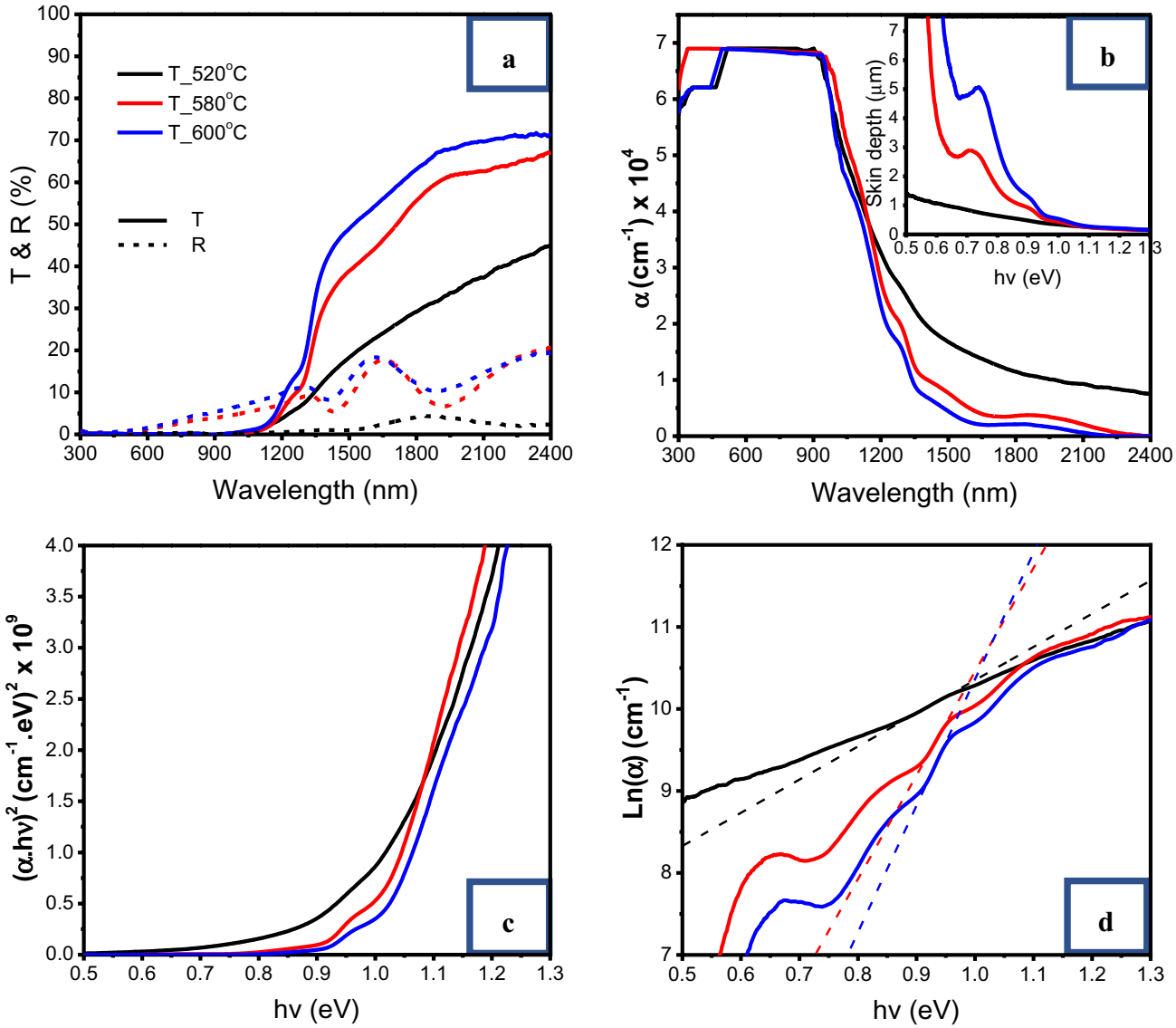

Fig. 8 Optical measurements: **a** transmission (continuous line) and reflectance (dashed line), **b** absorption coefficient intersected by Skin depth (small graph), **c** Tauc's plot (direct transition $n = 1/2$), and **d** Urbach energy of CTS thin films sulfurized at different temperatures

sulfurization sample *T_520* °C has a low transmission and better light absorption in the IR region than higher temperature samples which may be due to the presence of high structural defects. In the visible region, the three samples showed a comparable absorption. Increasing the sulfurization temperature to 580 and 600 °C revealed no distinct change on optical bandgap as all samples have a monoclinic structure. However, the second bandgap Eg_2 due to the VBS phenomenon was hard to be detected in the *T_520* °C due to its lower crystallinity compared to the other two samples. The low crystallinity of *T_52* °C is associated with significantly higher band tail below optical bandgap energy than the high-temperature samples, as seen in Fig. 8c. In the second place, the soda-lime glass transformation temperature is around 580 °C [44], so it is not preferred to go higher than this temperature in the industrial field. For this reason, 580 °C is chosen as the preferred sulfurization temperature.

3.4 Effect of sulfur amount inserted in the sulfurization process

The effect of the sulfur amount used during the sulfurization process and its implications on the structural and optical properties of CTS films was studied. The change in sulfurization amount of 10 and 100 mg of sulfur powder was applied for the sample prepared at 50 W and 1.4 Pa at sulfurization temperature of 580 °C. Although the XRD patterns of these two samples shown in Fig. 9a exhibited the

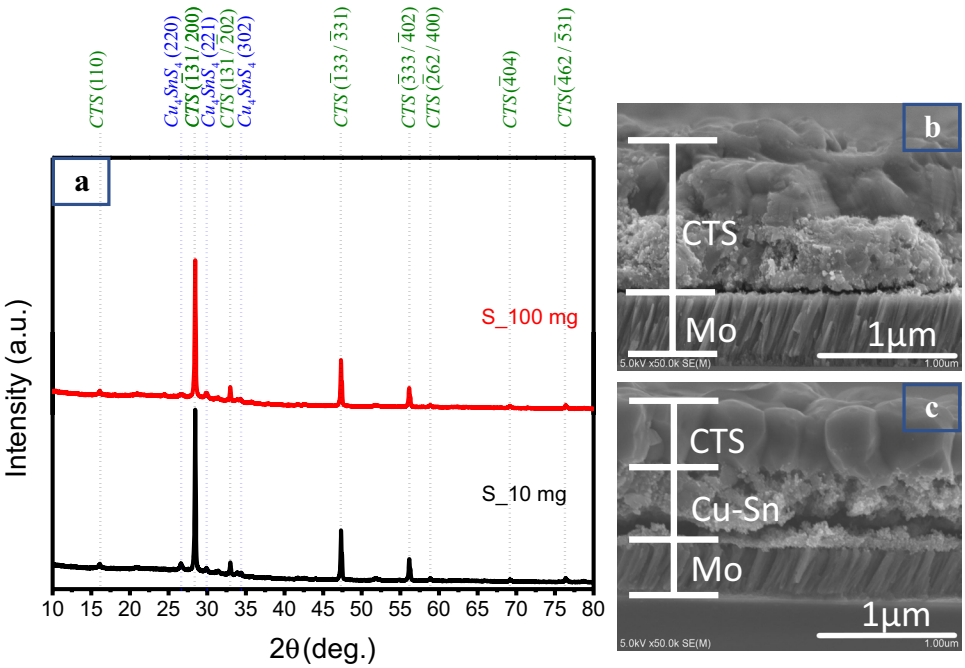

Fig. 9 **a** XRD pattern and cross-section SEM images of **b** *S_100 mg* and **c** *S_10 mg* samples sulfurized using different sulfur quantities

same sets of diffraction peaks, the SEM images are shown in Fig. 9b and c showing that the *S_10 mg* sample is not entirely sulfurized compared to *S_100 mg* one. It may be because XRD is collecting the average intensity of the diffractions. From the SEM micrograph in Fig. 9b, the uppermost surface of the *S_10 mg* sample is composed of large grains of CTS, while the lower part of the sample consists of small non-sulfurized Cu–Sn particles. This incomplete sulfurized Cu–Sn layer in the first place is attributed to the insufficient sulfur amount used during the sulfurization process that produces weak sulfur vapor pressure, which is not strong enough to penetrate deeply into the bottom of the Cu–Sn layer. The existence of a non-sulfurized Cu–Sn layer is an undesirable phenomenon as it is expected to inhibit the charge transfer across the CTS/Mo interface leading to inferior photovoltaic performance. Differently, the *S_100 mg* sample fabricated with a higher sulfur vapor pressure showed a deeper sulfurization, as can be inferred from the large CTS grains that protracted along the whole cross section of the sample as seen in Fig. 9b. Hence, using a copious amount of sulfur powder during the sulfurization process is essential to guarantee the complete sulfurization of the entire sample in order to achieve better photovoltaic performance.

Photoluminescence (PL) measurement as a valuable technique was employed to evaluate the optical quality of CTS thin-film samples fabricated with the best-chosen preparation conditions [45]. The PL measurements were performed on solar cell devices with SLG\Mo\CTS\CdS\ZnO\ZnO:Al configuration with 0V bias voltage at room temperature, and the acquired spectra are presented in Fig. 10a. The device fabricated based on the *S_10 mg* sample showed a very weak near-band-edge PL peak around 1300 nm (~ 0.95 eV). Considerably, the device fabricated with the *S_100 mg* sample showed a PL peak that is five to six times higher in intensity than that of the *S_10 mg*. The high PL signal attained by *S_100 mg* device demonstrates its superior optical quality as a consequence of minimizing the structural defects and secondary phases by the action of complete sulfurization resulting. Moreover, the high PL signal refers to the suppressed surface recombination rate indicating the successful passivation of the surface defects with a CdS buffer layer.

The solar cell (*J–V*) measurements asserted on the obtained PL results such that three TFSC devices based on the *S_10 mg* CTS sample showed a very weak photoresponse and yielded almost zero PCE (not shown here). On the other hand, another three TFSC devices assembled with the *S_100 mg* CTS sample showed a significant photoresponse and exhibited a high PCE of 1.94%, as shown in Fig. 10b. The high short-circuit current density (J_{SC}) value of 35.59 mA/cm^2 obtained from the undoped CTS-based solar cell prepared under the optimized condition is considerably superior to the values obtained from the undoped CTS-based solar cell prepared by sputtering [12, 17, 46], sequential evaporation [20], and also solution-processed [47] methods. The basis for such high J_{SC} value is the photocarriers generation over a wide range of the solar spectrum, as is revealed by the UV–Vis measurements. Also, it can be attributed to the effective charge collection and suppressed recombination loss aroused from the swift charge transfer across the CTS/Mo and the CTS/CdS interfaces along with fewer structural defects. The relatively low values of the open-circuit voltage (V_{OC}) = 159.7 mV and the low fill factor

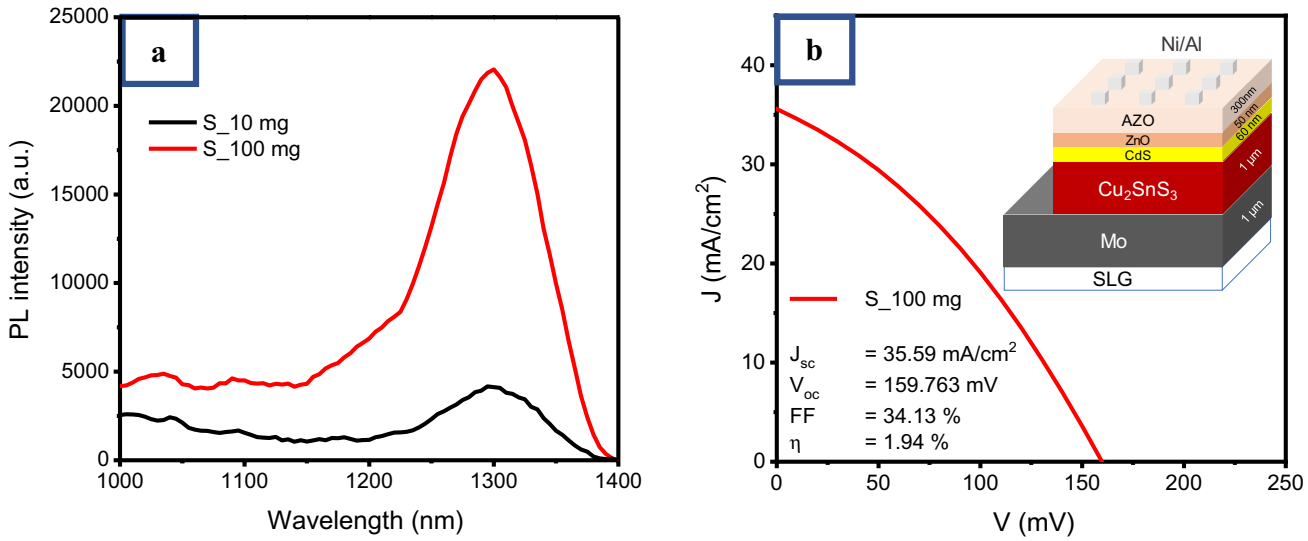

Fig. 10 **a** Photoluminescence response and **b** *J–V* curve for CTS samples sulfurized using different sulfur amounts intersected by fabricated solar cell device diagram

(*FF*) = 34.1% are due to the usage of CdS buffer layer which forms TYPE-II heterostructure interface with the CTS layer [48]. However, the obtained V_{OC} and FF values are comparable to solar cell devices fabricated from the undoped CTS layer [17, 49, 50]. To improve the overall performance of the CTS solar cell, we have a confident that selecting and optimizing the other interlayers should be studied at the same time with the studying of the CTS absorbing layer.

4 Conclusions

In this study, Cu_2SnS_3 (CTS) thin films for solar cell applications were prepared by RF sputtering and sulfurization process with different experimental conditions. The influences of changing RF sputtering (deposition power and pressure) and sulfurization (temperature and sulfur amount) parameters on the structural and optical properties of the fabricated thin films were carefully investigated. Under the experimental working conditions, the crystallographic structure of all samples was identified as a monoclinic CTS phase. Increasing RF sputtering power was led to an increase in the formation of Sn-based secondary phases. The increasing sputtering pressure leads to an increase in the unfavorable surface droplets and blistering. Thus, moderate sputtering power of 50 W and low pressure of 1.4 Pa is highly recommended to obtain a high-quality CTS layer for solar cell application. The high sulfurization temperature along with excess sulfur amount has been proven as the preferred sulfurization conditions for CTS crystallinity and thin-film surface morphology. The optical properties showed an independent energy bandgap on the sputtering pressure. The CTS thin film prepared at 1.4 Pa attained Urbach energy of ~ 68.8-meV and exhibited the highest absorption coefficient and the appropriate skin depth at the fundamental optical bandgap among the samples. Based on the optimum properties of the synthesized CTS, a solar cell device of the CTS layer was fabricated. This cell achieved a very high short-circuit current of 35.59 mA/cm^2 that is considered one of the best-recoded values of undoped CTS-based solar cells. When CdS buffer layer was used, a power conversion efficiency of 1.94% was also achieved because of TYPE-II heterostructure CdS makes with the CTS. Hence, employing the TYPE-I heterostructure interface along with precisely sputtered CTS absorber layer via choosing the proper n-type buffer layer is expected to yield a remarkable cutting-edge toward the commercialization of high-performance CTS-related thin-film solar cells.

Acknowledgements The authors would like to express their sincere gratitude to the Ministry of Higher Education (MOHE) – Egypt for their financial support and Tokyo University of Science - Noda Campus for offering the facilities and tools contribution.

Funding This work was funded by the Ministry of Higher Education (MOHE) – Egypt and supported by the Tokyo University of Science - Noda Campus by offering the facilities and tools.

Data availability The data that support the findings of this study are available from the corresponding author, Mohamed S. Abdel-Latif, upon reasonable request.

Compliance with ethical standards

Conflict of interest The authors declare that they have no conflict of interest.

References

1. Y. Hamakawa, *Thin-Film Solid Cells* (Springer, New York, 2004), pp. 1–14
2. D.J. Feldman, R.M. Margolis, Q4 2018/Q1 2019 Solar Industry Update (National Renewable Energy Lab.(NREL), Golden, CO (United States) (2019)
3. M.A. Green, E.D. Dunlop, D.H. Levi, J. Hohl-Ebinger, M. Yoshita, A.W.Y. Ho-Baillie, Prog. Photovoltaics Res. Appl. **27**, 565 (2019)
4. T. Bayazıt, M.A. Olgar, T. Küçükömeroğlu, E. Bacaksız, M. Tomakin, J. Mater. Sci. Mater. Electron. **30**, 12612 (2019)
5. S. Abdelhaleem, A.E. Hassanien, R. Ahmad, M. Schuster, A.H. Ashour, M. Distaso, W. Peukert, P.J. Wellmann, J. Electron. Mater. **47**, 7085 (2018)
6. A.C. Lokhande, K.V. Gurav, E. Jo, M. He, C.D. Lokhande, J.H. Kim, Opt. Mater. (Amst). **54**, 207 (2016)
7. G. Sunny, T. Thomas, D.R. Deepu, C.S. Kartha, K.P. Vijayakumar, Optik (Stuttg) **144**, 263 (2017)
8. Q. Chen, Z. Jia, H. Yuan, W. Zhu, Y. Ni, X. Zhu, X. Dou, J. Mater. Sci. Mater. Electron. **30**, 4519 (2019)
9. A. Nagoya, R. Asahi, R. Wahl, G. Kresse, Phys. Rev. B **81**, 113202 (2010)
10. M.S.A. Latif, N.M. Shaalan, A. A. El-Moneim, Key Engineering Materials. Trans Tech Publ, pp. 62–66 (2018)
11. J. Wu, C. Gao, L. Han, S. Shen, M. Jia, L. Wang, L. Jiang, F. Liu, J. Mater. Sci. Mater. Electron. **30**, 4378 (2019)
12. R. Chierchia, F. Pigna, M. Valentini, C. Malerba, E. Salza, P. Mangiapane, T. Polichetti, A. Mittiga, Phys. Status Solidi **13**, 35 (2016)
13. K. Tanaka, T. Maeda, H. Araki, Sol. Energy **199**, 143 (2020)
14. Y. Kim, I.-H. Choi, S.Y. Park, Thin Solid Films **666**, 61 (2018)
15. S.A. Zaki, M.I. Abd-Elrahman, A.A. Abu-Sehly, N.M. Shaalan, M.M. Hafiz, Mater. Sci. Semicond. Pro. **115**, 105123 (2020)
16. N. Thota, M. Kumar, M. Vishwakarma, B.R. Mehta, Thin Solid Films **677**, 62 (2019)
17. E.S. Hossain, P. Chelvanathan, S.A. Shahahmadi, B. Bais, M. Akhtaruzzaman, S.K. Tiong, K. Sopian, N. Amin, Sol. Energy **177**, 262 (2019)
18. H.D. Shelke, A.C. Lokhande, J.H. Kim, C.D. Lokhande, J. Alloys Compd. **831**, 154768 (2020)
19. K. Tanaka, M. Kowata, F. Yoshihisa, S. Imai, W. Yamazaki, Thin Solid Films **697**, 137820 (2020)
20. M. Nakashima, J. Fujimoto, T. Yamaguchi, M. Izaki, Appl. Phys. Express **8**, 42303 (2015)
21. D. Avellaneda, M.T.S. Nair, P.K. Nair, J. Electrochem. Soc. **157**, D346 (2010)
22. E.S. Hossain, P. Chelvanathan, S.A. Shahahmadi, M.T. Ferdaous, B. Bais, S.K. Tiong, N. Amin, Chalcogenide Lett. **15**, 499 (2018)
23. Y. Zhao, X. Han, B. Xu, C. Dong, J. Li, X. Yan, J. Mater. Sci. Mater. Electron. **30**, 17947 (2019)
24. P.R. Guddeti, S. Gedi, K.T.R. Reddy, Mater. Sci. Semicond. Process. **86**, 164 (2018)
25. Q. Zhang, H. Deng, J. Yu, B. Xu, J. Tao, P. Yang, L. Sun, J. Chu, Mater. Lett. **228**, 447 (2018)
26. M.R. Pallavolu, C.-D. Kim, V.R.M. Reddy, S. Gedi, C. Park, Sol. Energy **188**, 209 (2019)
27. H. Metin, R. Esen, J. Cryst. Growth **258**, 141 (2003)
28. F.I. Ezema, Y. Kayama, I.C. Amaechi, T. Hiramatsu, A.C. Nwanya, R.U. Osuji, M. Malik, M. Sugiyama, Chalcogenide Lett. 11, (2014)
29. K.-Y. Chan, B.-S. Teo, J. Mater. Sci. **40**, 5971 (2005)
30. K. Suzuki, J. Chantana, T. Minemoto, Appl. Surf. Sci. **414**, 140 (2017)
31. W. Wang, H. Shen, H. Yao, J. Li, J. Jiao, J. Mater. Sci. Mater. Electron. **26**, 1449 (2015)
32. Y. Dong, J. He, X. Li, Y. Chen, L. Sun, P. Yang, J. Chu, J. Alloys Compd. **665**, 69 (2016)
33. U. Chalapathi, B. Poornaprakash, S.-H. Park, Vacuum **131**, 22 (2016)
34. J. De Wild, E. Kalesaki, L. Wirtz, P.J. Dale, Phys. Status Solidi (RRL)–Rapid Res. Lett. **11**, 1600410 (2017)
35. I.G. Orletskii, M.N. Solovan, F. Pinna, G. Cicero, P.D. Mar'yanchuk, E.V. Maistruk, E. Tresso, Phys. Solid State **59**, 801 (2017)
36. I.M. El Radaf, H.Y.S. Al-Zahrani, A.S. Hassanien, J. Mater. Sci. Electron. **31**, 3228 (2020)
37. A.S. Hassanien, A.A. Akl, Superlattices Microstruct. **89**, 153 (2016)
38. A.S. Hassanien, A.A. Akl, J. Alloys Compd. **648**, 280 (2015)
39. A.S. Hassanien, I.M. El, Radaf, Phys. B Condens. Matter **585**, 412110 (2020)
40. D.S. Arteev, A.V. Sakharov, E.E. Zavarin, W.V. Lundin, A.N. Smirnov, V.Y. Davydov, M.A. Yagovkina, S.O. Usov, A.F. Tsatsulnikov, J. Phys. Conf. Ser. **1135**, 012050 (2018)
41. A.S. Hassanien, A.A. Akl, Phys. B Condens. Matter **576**, 411718 (2020)
42. P.M. Kaminski, S. Yilmaz, A. Abbas, F. Bittau, J.W. Bowers, R.C. Greenhalgh, J.M. Walls, In: proceedings of the 2017 IEEE 44th Photovolt. Spec. Conf. (IEEE, 2017), pp. 3430–3434 (2017)
43. P. Bras, J. Sterner, C. Platzer-Björkman, J. Vac. Sci. Technol. A Vac. Surf. Film **33**, 61201 (2015)
44. M.I. Ojovan, K.P. Travis, R.J. Hand, J. Phys. Condens. Matter **19**, 415107 (2007)
45. S. Shirakata, K. Ohkubo, Y. Ishii, T. Nakada, Sol. Energy Mater. Sol. Cells **93**, 988 (2009)
46. J. Chantana, K. Tai, H. Hayashi, T. Nishimura, Y. Kawano, T. Minemoto, Sol. Energy Mater. Sol. Cells **206**, 110261 (2020)
47. G.Y. Ashebir, C. Dong, J. Chen, W. Chen, R. Liu, Q. Zhao, Z. Wan, M. Wang, J. Phys. D. Appl. Phys. **53**, 115101 (2020)
48. S. Sato, H. Sumi, G. Shi, M. Sugiyama, Phys. Status Solidi **12**, 757 (2015)
49. M. He, A.C. Lokhande, I.Y. Kim, U.V. Ghorpade, M.P. Suryawanshi, J.H. Kim, J. Alloys Compd. **701**, 901 (2017)
50. J.Y. Lee, I.Y. Kim, M.P. Surywanshi, U.V. Ghorpade, D.S. Lee, J.H. Kim, Sol. Energy **145**, 27 (2017)